

Additive manufacturing of non-assembly deployable mechanisms for the treatment of large bony defects

Leeflang, M. A.; Bobbert, F. S.L.; Zadpoor, A. A.

DOI

[10.1016/j.addma.2021.102194](https://doi.org/10.1016/j.addma.2021.102194)

Publication date

2021

Document Version

Final published version

Published in

Additive Manufacturing

Citation (APA)

Leeflang, M. A., Bobbert, F. S. L., & Zadpoor, A. A. (2021). Additive manufacturing of non-assembly deployable mechanisms for the treatment of large bony defects. *Additive Manufacturing*, 46, Article 102194. <https://doi.org/10.1016/j.addma.2021.102194>

Important note

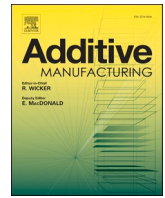
To cite this publication, please use the final published version (if applicable). Please check the document version above.

Copyright

Other than for strictly personal use, it is not permitted to download, forward or distribute the text or part of it, without the consent of the author(s) and/or copyright holder(s), unless the work is under an open content license such as Creative Commons.

Takedown policy

Please contact us and provide details if you believe this document breaches copyrights. We will remove access to the work immediately and investigate your claim.



Research Paper

Additive manufacturing of non-assembly deployable mechanisms for the treatment of large bony defects

M.A. Leeflang^{*,1}, F.S.L. Bobbert¹, A.A. Zadpoor

Department of Biomechanical Engineering, Delft University of Technology, Mekelweg2, Delft 2628CD, The Netherlands

ARTICLE INFO

Keywords:

Non-assembly mechanisms
Selective laser melting
Deployable structures
Bone regeneration

ABSTRACT

Porous biomaterials are often used to treat large bony defects or fractured vertebrae. Most of such biomaterials are made of metals and their alloys and have a pre-defined, fixed shape. Due to their predefined fixed shape, however, they are not suitable for implantation through minimally invasive surgical procedures. To overcome this problem, we designed three different deployable non-assembly mechanisms, which were manufactured using selective laser melting. These deployable geometries, including a bicapped cube, a bicapped trigonal antiprism, and a bicapped square antiprism, possess a large aspect ratio in their retracted state. Upon the application of an external force, they expand radially into their deployed load-bearing configuration. Using non-assembly manufacturing, revolute joints, wavelike elements, rigid rods and restrictions could be integrated into the design. The designs were manufactured in such a way that the least amount of support structures was required during the fabrication process. Additionally, the deployable structures were functional immediately after printing. Mechanical tests were performed to determine the forces required to deploy the designed structures and to determine their failure load. A maximum change of $322 \pm 7\%$ in the circumdiameter was found for the bicapped trigonal antiprism while the bicapped square antiprism showed the largest reduction in the height ($61 \pm 1\%$). A maximum force of 10.3 ± 1.6 N was required during the deployment process of the bicapped square antiprism 3. The bicapped antiprisms could support up to 1212 ± 45.5 N before they failed, while the bicapped cubes failed under a force of 232 ± 5.5 N. The elongated geometry of our designs makes them ideal for implantation using minimally invasive surgical procedures. Given the fact that these are the first non-assembly deployable bone substitutes manufactured using selective laser melting, further studies are required to make them suitable as orthopedic implants.

1. Introduction

Bone tissue regeneration approaches often require the use of porous biomaterials for the treatment of large bony defects [1]. These bony defects are too large to be repaired by the cells inside our body and surgical intervention is required [2]. Although bone tissue substitutes such as autogenous and allogeneic tissue grafts are available, their limited supply [3,4], donor site morbidity [3], and the risk of viral and bacterial disease transmission [3,5] motivate the development of engineered and innovative replacements [3,4].

Various types of bone substitutes [2,6–8] have been fabricated using additive manufacturing (AM) techniques. Selective laser melting (SLM) is the most commonly used AM technique for the fabrication of porous biomaterials made of metals and their alloys, including titanium [9–12],

zinc [13–15], magnesium [16–18], and iron [19,20].

Although many types of porous biomaterials and (patient-specific) orthopedic implants have been manufactured using SLM [21], most of them have a pre-determined, fixed shape. Such voluminous, fixed-shape implants can hardly be implanted using minimally invasive surgery techniques. Minimally invasive surgeries, such as arthroscopy and laparoscopy [22,23] limit the damage to the body, require shorter recovery times [24], and lower the risk of post-operative complications [25,26]. This is due to the small incisions required to insert the medical devices into the body [23].

A potential solution for the high invasiveness of such orthopedic surgeries is the use of deployable implants, which are initially compact and can, thus, be implanted using minimally invasive surgical techniques. Upon the application of an external force, the structures can

* Corresponding author.

E-mail address: M.A.Leeflang@tudelft.nl (M.A. Leeflang).

¹ These authors contributed equally to this work

transform into their deployed configuration inside the defect. We have recently applied AM for the fabrication of deployable meta-implants [27,28]. While our previous designs demonstrate both the concept of deployability in meta-implants and the utility of AM, they generally require an assembly step. Such a step is labor-intensive, time-consuming, and makes it very challenging to upscale the production of such implants. Non-assembly AM could pave the way for the large-scale production of deployable meta-implants.

Recently, AM has been used for the fabrication of a limited number of non-assembly mechanisms [29–31], which are manufactured using a single-step fabrication process and are often made of rigid bodies and joints. Due to the design choices and the orientation of such mechanisms on the build platform, there is no need for an assembly step after fabrication [32,33]. The other advantages of this approach include unique functionalities, improved kinematic performance, and the integration of advanced features in the design process [31]. Two examples of non-assembly mechanisms manufactured using SLM are the CubeSat [34] and metallic clay [35]. The CubeSat is a cube ($10 \times 10 \times 10 \text{ cm}^3$) developed for space research. Although various CubeSat designs are available, Boschetto et al. [34] used SLM to manufacture an already-assembled CubeSat consisting of two half cubes connected by a hinge [34]. By integrating locating and locking features into the design, both halves are guided as the cube closes, thereby ensuring that they eventually attach to each other [34]. A more relevant concept for orthopedic applications is that of metallic clay, which we have recently proposed for shape-matching biomaterials [35]. Metallic clay is composed of a network of joints, spring-like elements, rigid rods, and locking mechanisms that work together to enable the shape-morphing and shape-locking behaviors of the mechanisms (analogous to the states of clay before and after firing, respectively) [35].

In this study, we propose a number of novel designs that make it possible to use SLM for non-assembly AM of deployable implants. We chose the treatment of fractured vertebrae and large bony defects in the pelvis as the model surgical challenges for which the deployable implants were designed. We designed the mechanisms such that they had a large aspect ratio in their retracted state. Upon the application of an external force, the elongated structures expand radially into their deployed configuration. We integrated different features to lock the deployed configuration of the specimens. Wavelike elements, revolute joints, and restrictions enable the reconfiguration and locking of the mechanisms. Additionally, we used specific design approaches and selected the build orientation in such a way that the minimum number of support structures were required during the manufacturing process. We then manufactured different designs using SLM and mechanically tested the resulting implants to determine their deployment force and their failure loads.

2. Materials and methods

2.1. Design

2.1.1. Components of the designs

Three different deployable geometries were designed, namely a bicapped trigonal antiprism, a bicapped square antiprism, and a bicapped cube (Fig. 1a, b). The bicapped antiprisms were constructed with connecting rods a and b along all the slanting edges of the geometry. No rods were placed along the edges of the base faces. At all vertices, clusters of revolute joints were positioned with a separate joint for every connecting rod. The axes of rotation of all joints were in parallel to the basal plane and perpendicular to the connecting rods.

Contrary to the bicapped antiprisms, the side faces of the bicapped cube did not consist of alternating isosceles triangles but of rectangles (Fig. 1a, b). In this geometry, the rods were positioned along the diagonals m and n with a revolute joint at the intersection, creating two mirrored isosceles triangles. No rods were placed at the vertical and horizontal edges.

The geometries can be deployed by compressing them at the proximal and distal vertices A and B , respectively (Fig. 1c). This action decreases the angle α of the lateral edge with the base diagonal of the bicapped structures and simultaneously increases the vertex angle γ of the isosceles triangles on the side faces. Consequently, the circumradius R of the triangle or square base face increases from its smallest value in the retracted state to its maximum value when $\alpha = 0^\circ$ (Figs. 1c, 2). By moving A and B further inwards, the circumradius reduces until A and B meet in the center and the deployed state of the geometry is reached. Pulling at A and B reverses the deployment process and leads to the retraction of the geometry.

2.1.2. Design variations

We varied the dimensions of the designed structures to study the effects of those dimensions on the kinematics and kinetics of the deployable meta-implants. The length of the connecting rod a determined the circumradius of the structure while the height is determined by the length of the connecting rod b or m and n for the bicapped antiprism and bicapped cube, respectively. Fig. 3d shows six bicapped square antiprisms, including three different lengths for the connecting rod a and two different lengths for the connecting rod b (Fig. 3a).

2.1.3. Evaluated design

In order to create a retracted configuration, a maximum circumradius, and a deployed state, restrictions were placed on the bearings of the revolute joints to limit the movement of the rods. The rods b and m and n of the antiprisms and the bicapped cube, respectively, were restricted in the deploying direction to a maximum circumradius of L_x . In addition, rods a were restricted at the retracted and deployed positions.

When comprising only rigid rods, the geometries can freely move between the retracted and deployed positions provided that the length of the connecting rods a is smaller or equal to the maximum restricted circumradius L_x . However, when they are longer than L_x , the geometry cannot move further towards the deployed position. Substituting these rigid rods connected to the proximal and distal vertices A and B with wavelike rods allows the rods to deform in the lateral direction. This deformation reduces the length of the wavelike rod to equal the circumradius and enables vertices A and B to be pushed through this position and reach the deployed, locked state.

Five configurations were prepared with a varying oversize of the wavelike rods (Fig. 1d). The oversize was defined as a / L_x where a is the length of the wavelike rods and L_x is the designed axis-to-axis distance between the paired revolute joint bearings at the maximum restricted circumradius, measured horizontally.

The changes in the specimen dimensions as a consequence of deployment were determined through the measurements of the height and circumdiameter of the specimens in their retracted and deployed configurations. Since the height reduced and the circumdiameter increased upon deployment, the reduction in the height and increase in the circumdiameter were determined as:

$$\text{reduction in height} = \left(1 - \frac{\text{deployed height}}{\text{retracted height}} \right) \times 100$$

and

$$\text{increase in circumdiameter} = \frac{\text{deployed circumdiameter}}{\text{retracted circumdiameter}} \times 100.$$

2.2. Manufacturing

The specimens were manufactured in-house using an SLM125 (Realizer GmbH, Germany) machine. As feedstock, plasma-atomized Ti6Al4V-ELI powder with a particle size between 10 and 45 μm (AP&C, Canada) was used. The build chamber was flushed with argon gas to ensure an oxygen level below 0.2% during printing. The substrate

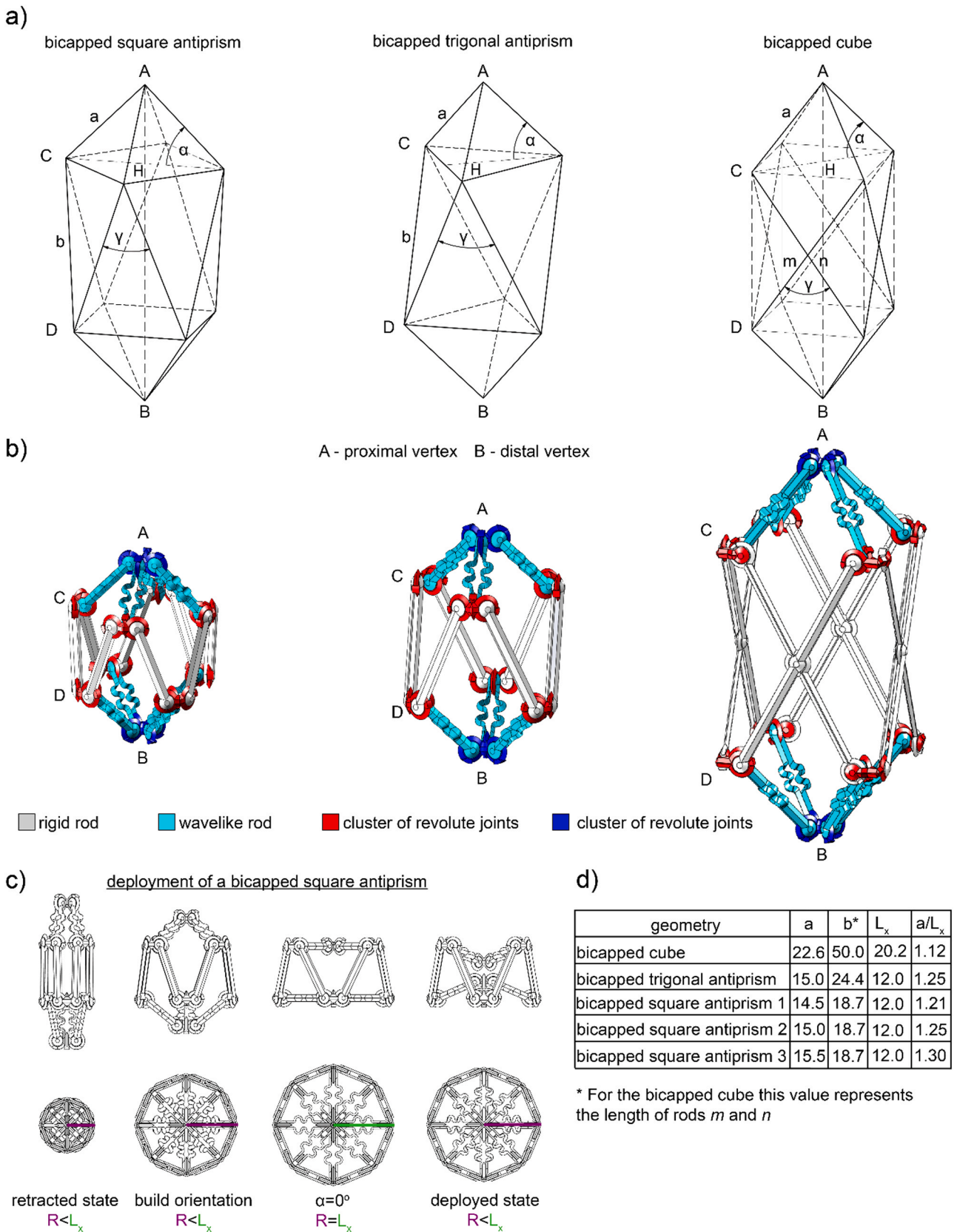


Fig. 1. a) The line drawings of the bicapped square antiprism, the bicapped trigonal antiprism, and the bicapped cube. b) The CAD models of the three geometries plotted in their configuration during the SLM process. Red: a cluster of revolute joints, Blue: the proximal and distal clusters of revolute joints, turquoise: wavelike rod, grey: rigid rod. c) The different states of a bicapped square antiprism during its deployment process with an indication of the circumradius R and the designed maximum circumradius L_x . d) The values of the length of the wavelike rods (a) [mm], the length of the rigid rods (b , m , and n) [mm], and the designed maximum circumradius L_x . (For interpretation of the references to colour in this figure legend, the reader is referred to the web version of this article.)

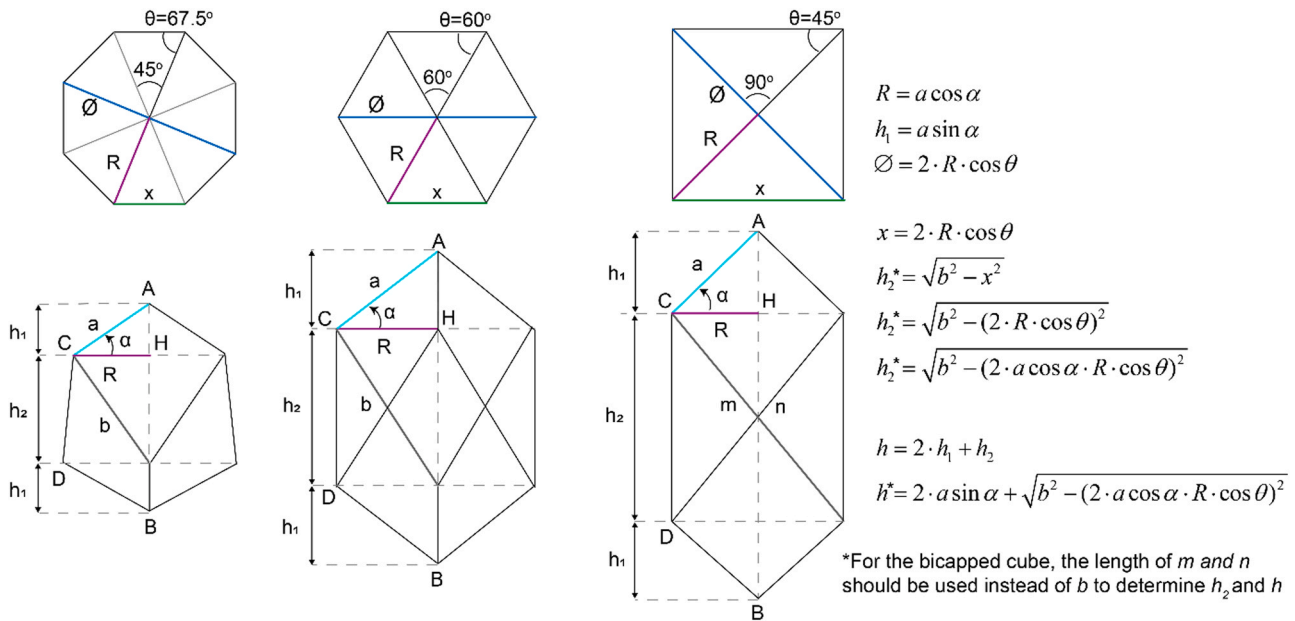


Fig. 2. Equations to determine the theoretical diameter and height of the different geometries from their maximum circumradius ($\angle ABH = 0^\circ$) to fully retracted. The top and side views of the bicapped square antiprism, the bicapped trigonal antiprism, and the bicapped cube.

plate, on which the specimens were built, was kept at 100 °C. The process parameters used for the contour and hatch are specified in Table 1.

After printing (Fig. 3b, c), the substrate supports were removed from all downward-facing, exterior surfaces of the specimens. The revolute joints of the specimens were designed in such a manner that support structures were not required for maintaining their clearance space. This is in contrast with traditional joints (e.g., traditional ball-and-socket joints) where support structures are required to ensure the different parts of the joints remain separate from each other. In order to remove the loose powder particles remaining in the joint clearance, the specimens were ultrasonically cleaned for 15 min.

2.3. Mechanical tests

2.3.1. Deployment forces

A Lloyd LR5K mechanical testing machine was used to determine the forces required to deploy the specimens. Compression tests were performed using a crosshead speed of 20 mm/min and a 100 N load cell. Before a specimen was compressed in order to deploy the specimen, it was attached to the machine using wire steel at its proximal and distal vertices (Figs. 4a, 5a).

Due to the different dimensions of the specimens, the maximum displacement of the crosshead varied per design. The tests were aborted after 42 mm, 44 mm, and 70 mm for the bicapped square antiprisms, bicapped trigonal antiprism, and the bicapped cube specimens, respectively. The deployment force measurements were repeated three times per specimen.

The forces taken from the force-displacement curves were $F_{firstpeak}$ (the force required to open the specimen), F_{max} (the force required to deform the wavelike elements to enable the locking process), and F_{lock} (the force required to bring the specimen into its load-bearing deployed state ($\angle ABH < 0^\circ$)).

2.3.2. Failure load

The failure loads of the specimens were measured in their deployed configuration to determine the maximum load that the specimens could support. The specimens were placed onto the bearing plate and a 5 kN load cell was connected to the crosshead to compress the specimens with a crosshead speed of 5 mm/min.

2.3.3. Fracture analysis

A sample of fracture surfaces were imaged on a JSM-IT100 (JEOL Ltd., Japan) scanning electron microscope (SEM). Secondary electron detection was used at an accelerating voltage of 10 kV. Before imaging, the specimens were gold sputtered.

3. Results

3.1. Change in dimensions

All specimens were measured in their retracted and deployed configurations (Table 2). The smallest increase in the circumdiameter ($185 \pm 40\%$) and smallest reduction in the height ($53 \pm 2\%$) were found for the bicapped cube specimens. The circumdiameter of the bicapped trigonal antiprism specimens increased the most ($322 \pm 7\%$) and the largest reduction in the height ($61 \pm 1\%$) was found for the bicapped square antiprism 3 specimens.

3.2. Mechanical tests

3.2.1. Deployment forces

The different lengths of the rigid and wavelike rods and the geometry of the specimens led not only to different mechanical behaviors but also to different ways of deployment (Figs. 3b, 4b). The bicapped cube specimens all started their deployment process by opening the proximal vertex and distal vertex simultaneously, which was followed by the inward movement and locking of the distal vertex. The inward movement and locking of the proximal vertex was always the last step in the deployment process (Fig. 4a). Further to this deployment sequence, the bicapped trigonal antiprism and bicapped square antiprism specimens also showed a sequence in which the inward movement and locking of the distal vertex was the last step in the deployment process. These different sequences of deployment showed different force-displacement curves (Figs. 4 and 5).

In the first stage of the deployment process, the bicapped square antiprism 3 specimens required the highest force ($F_{firstpeak} = 6.7 \pm 1.1$ N) to open either the proximal or distal vertex of the specimens. The bicapped cube specimens required the least force to open ($F_{firstpeak} = 1.5 \pm 1.4$ N) (Fig. 4b, c).

The force-displacement graphs of the sequence in which the locking

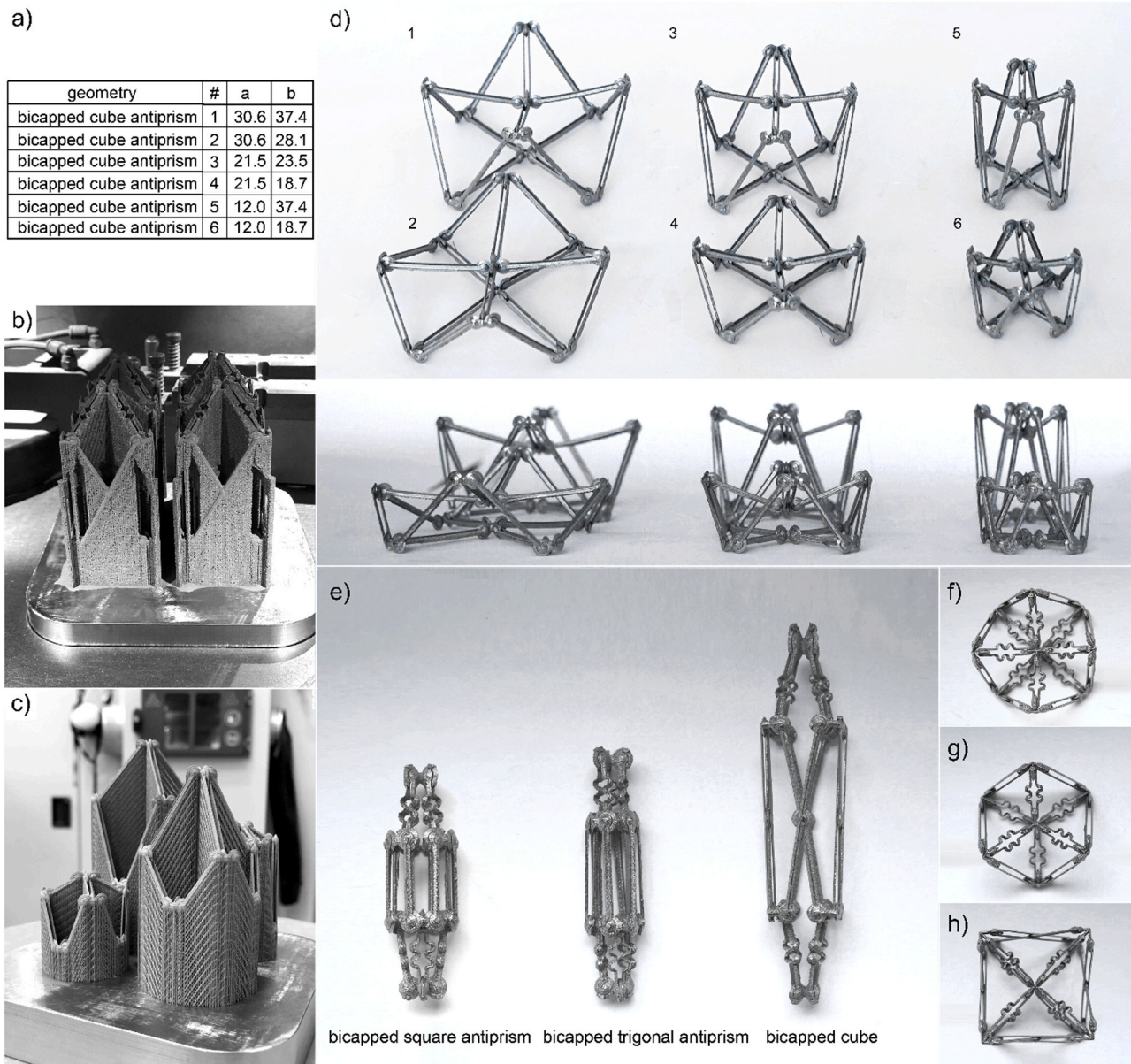


Fig. 3. a) The table listing the lengths of the connecting rods *a* and *b* with numbers corresponding to the bicapped square antiprisms designs presented. b) As-built bicapped cube specimens with wavelike and rigid connecting rods. c) As-built bicapped square antiprism specimens composed of solely rigid rods. d) SLM specimens in their retracted state: a bicapped square antiprism, a bicapped trigonal antiprism, and a bicapped cube. e) The top view of the deployed configuration of a bicapped square antiprism specimen. f) The top view of the deployed state of a bicapped trigonal antiprism specimen. g) The top view of the deployed configuration of a bicapped cube specimen.

Table 1
The contour and hatch parameters used in the laser scanning process.

Process parameters	Contour	Hatch
Slice height [μm]	50	50
Laser power [W]	88	88
Exposure time [μs]	20	5
Point distance [μm]	10	10
Scanning strategy	-	90° alternating
Hatch distance [μm]	-	150
Hatch offset [μm]	-	80

of the proximal vertex is the last step in the deployment process (Fig. 4b) showed that the wavelike elements of bicapped square antiprism 3 require the most force to be compressed ($F_{max} = 10.3 \pm 1.6$ N).

This geometry is followed by the bicapped cube specimens ($F_{max} =$

6.3 ± 2.4 N), bicapped square antiprism 2 ($F_{max} = 2.6 \pm 0.3$ N), bicapped square antiprism 1 ($F_{max} = 2.2 \pm 0.6$ N), and finally the bicapped trigonal antiprism ($F_{max} = 1.3 \pm 0.2$ N) specimens (Fig. 4b, c). The bicapped square antiprism 3, bicapped square antiprism 2, and the bicapped cube specimens showed a negative force of $F_{lock} = -1.6 \pm 1.2$ N, $F_{lock} = 0 \pm 0.3$ N, and $F_{lock} = -1 \pm 0.8$ N respectively, during the locking of the proximal vertex.

Similar to the deployment sequence in which the locking of the proximal vertex was the last step of the deployment process, the bicapped square antiprism 3 specimens required the highest force to completely open the proximal and distal vertices ($F_{firstpeak} = 4.6 \pm 0.6$ N) and to deform the wavelike rods ($F_{max} = 8.7 \pm 0.1$ N) when the inward movement of the distal vertex was the last step of the deployment process (Fig. 5b, c). Contrary to the forces in the final stage of the deployment process of the bicapped square antiprism 3 specimens, no negative forces were observed during the locking of the distal

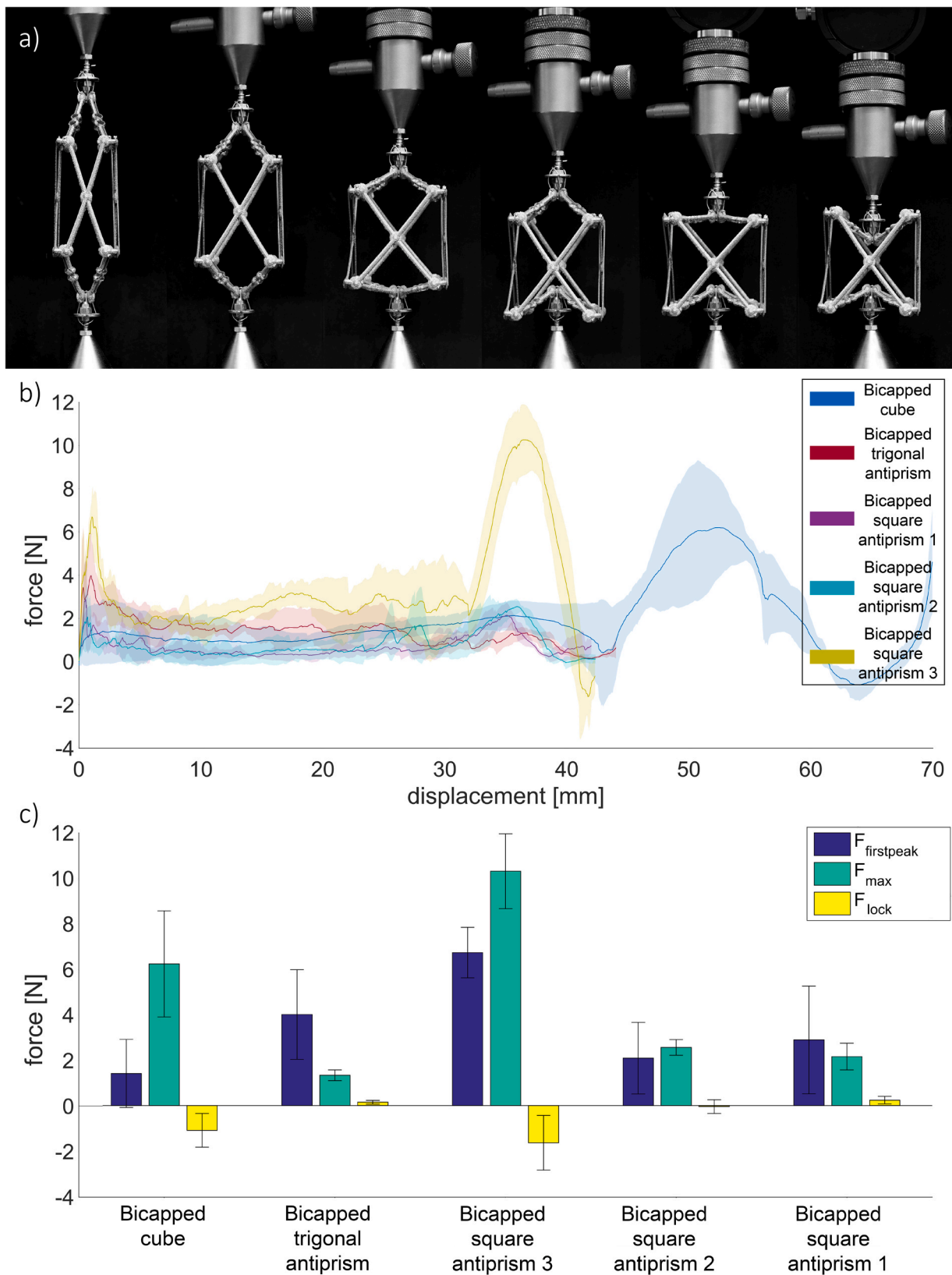


Fig. 4. The results of the compression tests where the proximal vertex moves inward later than the distal vertex. a) An example of a bicapped cube compression where the distal vertex opens first, followed by the inward movement of the distal vertex and finally the inward movement of the proximal vertex. b) The force-displacement curves of the different structures. c) A bar plot with $F_{firstpeak}$, F_{max} , and F_{lock} and the corresponding standard deviations measured for all the deployable structures studied here.

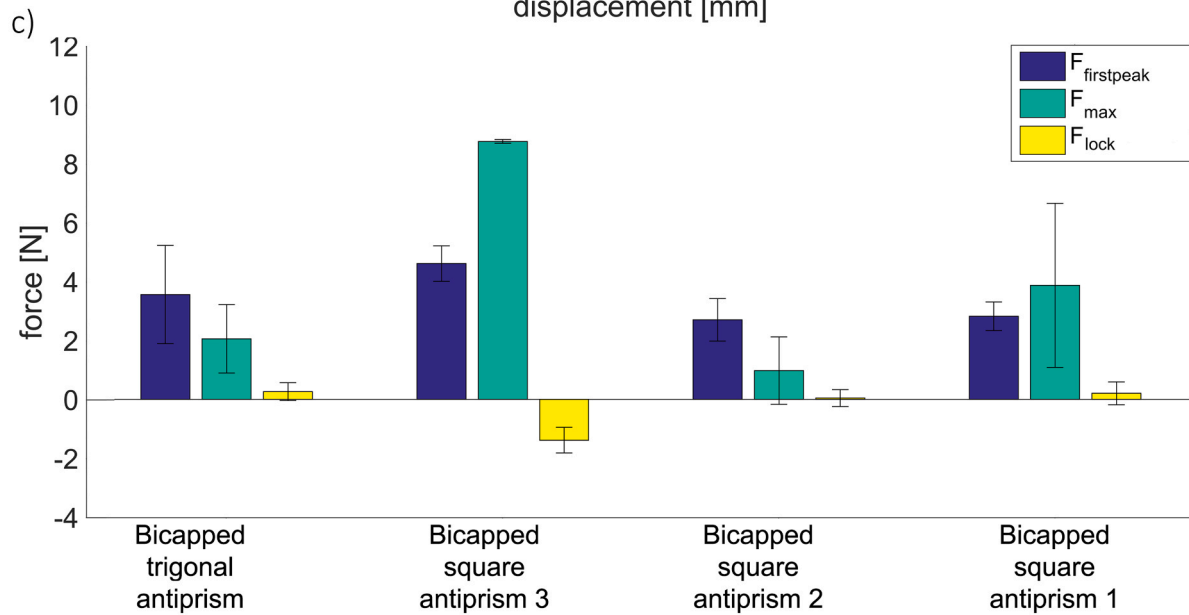
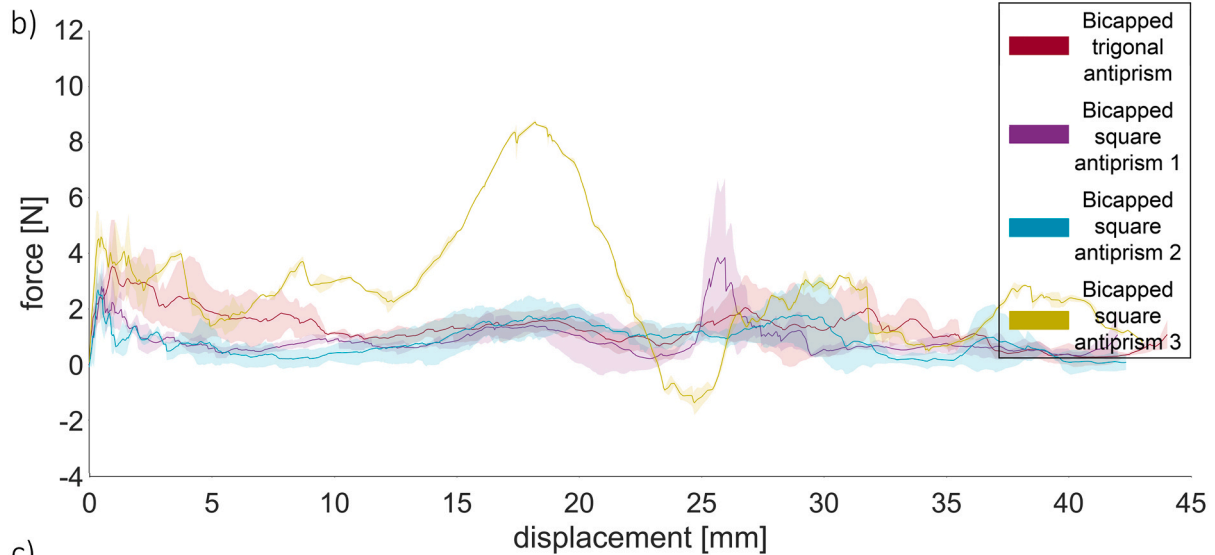
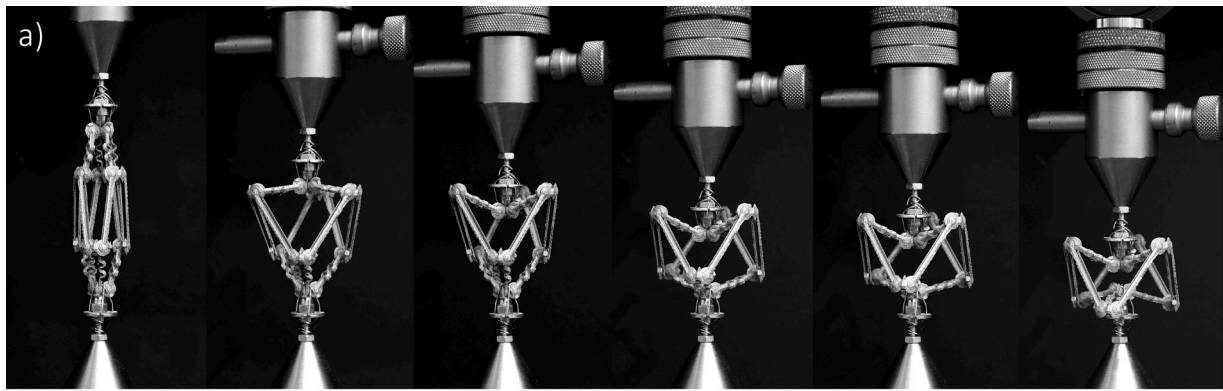


Fig. 5. The results of the compression tests where the distal vertex moves inward after the proximal vertex. a) An example of the compression of a bicapped trigonal antiprism specimen where the proximal vertex opens first, followed by the inward movement of the proximal vertex and finally the inward movement of the distal vertex. b) The force-displacement curves of the different structures. c) A bar plot with $F_{firstpeak}$, F_{max} , and F_{lock} and the corresponding standard deviations measured for all the deployable structures studied here.

vertex (F_{lock}) of the bicapped trigonal antiprism, bicapped square antiprism 1, and bicapped square antiprism 2 specimens (Fig. 5b, c).

3.2.2. Failure loads

The mechanical tests performed to determine the failure loads of the specimens showed that the bicapped square antiprism 3, bicapped square antiprism 2 and bicapped square antiprism 1 specimens failed

Table 2

The dimensions of the specimens in their retracted and deployed states.

Geometry	Retracted		Deployed		Change in dimensions	
	Height [mm]	Circumradius [mm]	Height [mm]	Circumradius [mm]	Height [%]	Circumradius [%]
bicapped cube	97.6 ± 2.7	31.4 ± 5.7	45.8 ± 0.9	56.6 ± 1.1	53 ± 2	185 ± 40
bicapped trigonal antiprism	60.1 ± 0.1	12.8 ± 0.3	25.3 ± 0.1	41.1 ± 0.1	58 ± 0	322 ± 7
bicapped square antiprism 1	53.1 ± 0.2	16.0 ± 0.3	22.3 ± 0.7	39.2 ± 0.2	58 ± 1	245 ± 4
bicapped square antiprism 2	54.0 ± 0.3	16.0 ± 0.2	21.9 ± 0.1	40.4 ± 0.9	59 ± 0	253 ± 7
bicapped square antiprism 3	55.1 ± 0.2	16.7 ± 0.6	21.4 ± 0.3	40.7 ± 0.2	61 ± 1	244 ± 9

after applying 1212 ± 45.5 N, 1074 ± 273.6 N, and 1110 ± 185.9 N, respectively (Fig. 6). The bicapped trigonal antiprism and bicapped cube specimens failed at much lower loads (547 ± 64.1 N and 232 ± 5.5 N, respectively) (Fig. 6).

The failure mechanism for all structures were similar. Under loading, the rigid rods of the bicapped antiprisms bent and buckled until they fractured at the middle of the rod where the maximum deflection and bending stresses were present (Fig. 6a). For the bicapped cubes, however, a revolute joint connects the two rigid rods at the center. Therefore, the rigid rods fractured at a location close to the revolute joint. All wavelike rods remained intact. The representative fractographs of the specimens (Fig. 7) show predominantly smooth fracture surfaces at the perimeter of the rigid rods, indicating brittle fracture. However, the fracture surfaces of the bicapped square antiprism and the bicapped cube also contained areas with shallow dimples (Fig. 7a,c). These results suggest that plastic deformation in these areas led to ductile fracture of the rods.

4. Discussion

In this study, we presented the concept of *non-assembly* AM deployable mechanisms for application as orthopedic implants. An important aspect of these new designs is that they can be manufactured from metals using a powder bed fusion process (i.e., SLM) and without a need for internal supports (i.e., in the clearance space of the joints). Both the non-assembly nature of the designs and the fact that these structures

were manufactured from metals distinguish this study from our previous study where we introduced the concept of deployable meta-implants for the first time [27]. The non-assembly nature of the designs means that their manufacturing step is practical and straightforward to upscale, while the fact that they are made from metals means that they exhibit much higher mechanical properties as compared to the previous polymeric designs.

4.1. Deployability

The deployable porous biomaterials presented in this study could all reconfigure from an elongated retracted state to a radially expanded and lengthwise shortened deployed configuration. The small circumradius of the retracted specimens makes it possible to insert the porous biomaterials via a small incision into the body. A large standard deviation of 40% was observed for the increase in circumradius of the bicapped cube specimens. This could be explained by the much smaller circumradius of one of the specimens in its retracted state. Since all specimens were manufactured simultaneously and were based on the same design, this behavior seems to be an effect of the SLM process. The bicapped trigonal antiprism specimens had the smallest circumradius in their retracted state, which can be explained by the number of joint bearings at the sides of the geometry. The joint bearings of the antiprism specimens touch each other in their retracted configuration. Since the bicapped trigonal antiprism specimens have fewer joint bearings, these specimens can be made smaller than the bicapped square antiprism

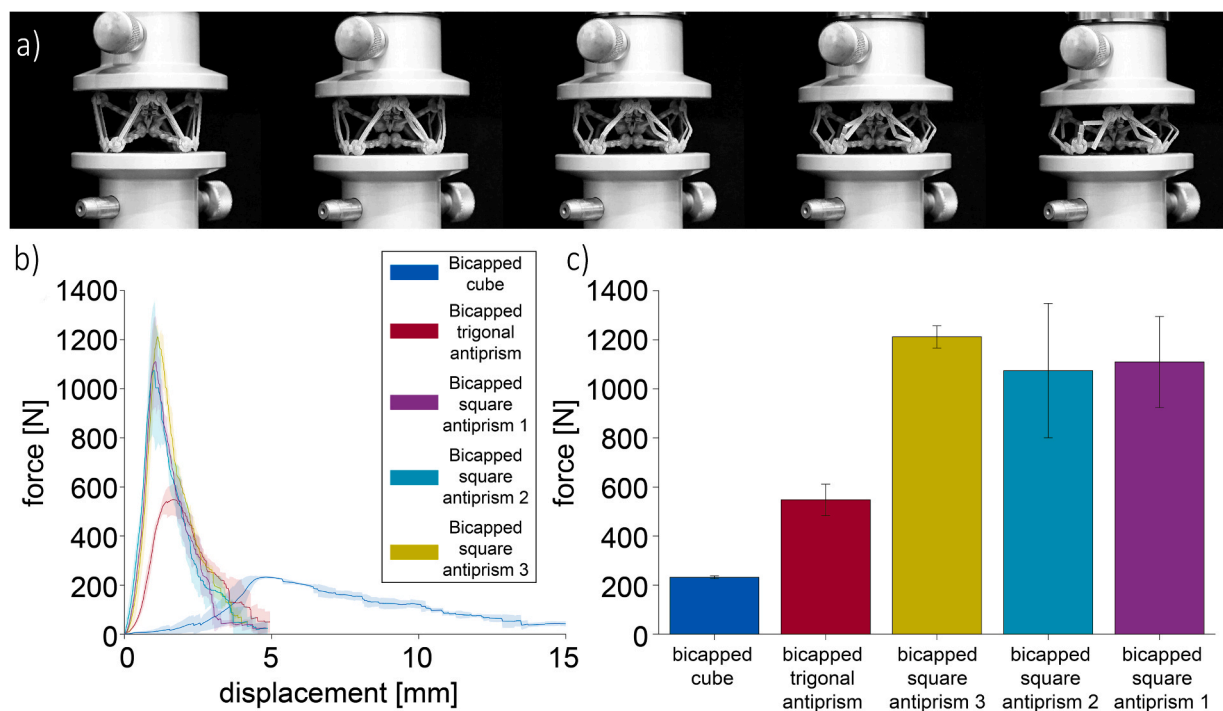


Fig. 6. The results of the compression to failure tests. a) An example of a bicapped square antiprism specimen being compressed. b) The force-displacement curves of the different structures. c) A bar plot with the load to failure of the different geometries.

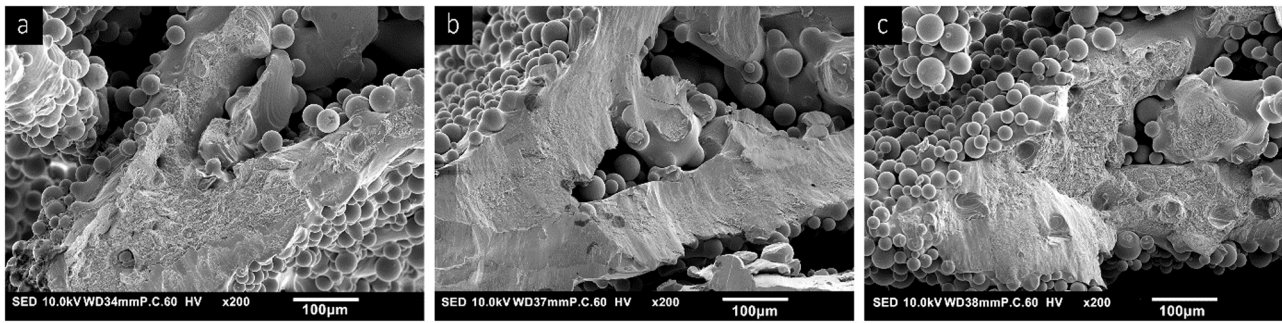


Fig. 7. Fractographs of the failed structures. a) bicapped square antiprism, b) bicapped trigonal antiprism, c) bicapped cube.

specimens. The circumdiameters of all the specimens in their deployed state are dependent on the length of the wavelike rods (a). Due to the similar length of these rods for the antiprism specimens, the circumdiameter of the deployed state of these specimens is comparable. Due to the smaller radial dimensions in its retracted state, the bicapped trigonal antiprism geometry would be the most suitable for implantation using minimally invasive surgery.

4.2. Mechanical performance

4.2.1. Deployment forces

This concept of deployable mechanisms as potential porous biomaterials for the treatment of large bony defects using minimally invasive surgery requires easy deployment when brought into the bone defect. The deployable structures proposed in this paper are easily reconfigurable by applying a compressive force at their proximal and distal vertices. Although our designs can be easily deployed by hand or by a mechanical testing machine with a maximum force of 10.3 ± 1.6 N, a dedicated minimally invasive surgery tool would be required to deploy such type of implants inside the body. The maximum force required during the deployment process was reached during the deformation of the wavelike elements at the point where the maximum circumradius is reached ($\alpha = 0^\circ$). This means that the maximum force can be controlled by adjusting the oversize, which depends on the length of the wavelike rods a and the designed maximum circumradius L_x . Longer wavelike rods need to deform more than shorter wavelike rods when L_x is kept constant. In Fig. 4b and c, it can be seen that the bicapped square antiprisms with smaller values for a , indeed, require a lower maximum force when the inward movement of the proximal vertex is the last step in the deployment process. However, this theory does not seem to hold when the inward movement of the distal vertex is the last step in the deployment process. Moreover, the geometry of the deployable structure affects the force required to deform the wavelike rods at the point where the maximum circumradius is reached. While the specimens designed based on the bicapped trigonal antiprism and bicapped square antiprism 2 have the same oversize value, more force is required to deform the wavelike rods of the latter type. This could be explained by the number of the wavelike rods connected to the proximal and distal vertices. Only three wavelike rods need to be deformed simultaneously in the bicapped trigonal antiprism while four rods need to be deformed in the bicapped square antiprism.

Our observation of a negative force during the deployment of the bicapped square antiprism 3, bicapped square antiprism 2, and the bicapped cube specimens show that there is a snap-through behavior present in some deployment sequences. This effect is enabled by the deformation of the wavelike rods connected to the proximal and distal vertices, which act as bi-stable beams at the point where the maximum circumradius L_x is reached. Bi-stable beams can snap from one load-bearing configuration to another when the load applied reaches a critical level [36]. In one of our previous studies [27], we used this type of instability to develop our first concepts of deployable meta-implants.

4.2.2. Failure loads

Large bony defects can occur at any location, either load-bearing or not. The deployed structures evaluated in this paper could support loads up to 1212 ± 45.5 N before bending or buckling occurs. This is a significant improvement as compared to the load-bearing properties of our previously developed concepts for deployable implants and is already within the lower range of the compressive loads reported in the literature for spinal compression (relevant for the treatment of fractured vertebrae) [37]. Our multi-stable deployable PLA (polylactic acid) meta-biomaterials made of bi-stable elements [27] and bi-stable panels [28] could respectively support loads of ≈ 10 N or ≈ 35 N, before retraction would occur. This large difference can be mainly explained by the definition of ‘deployed configuration’ of our PLA specimens and these non-assembly mechanisms. The PLA specimens were defined as deployed when they were expanded in all directions, while these non-assembly mechanisms are defined as deployed when they are radially expanded and lengthwise shortened. In their deployed state, the non-assembly mechanisms are, therefore, already retracted in their axial direction and locked in this deployed configuration. Both types of deployment (i.e., deployment in all directions or radial deployment upon axial compression) could potentially be applied as deployable bone substitutes. While our previous designs of multi-stable structures and foldable designs can be transported in a compact state in all directions, these non-assembly mechanisms can be easily inserted into the body due to their elongated shape in their retracted configuration. It is clear that the designs with the second type of deployment are superior in terms of load-bearing properties.

The force-displacement curves show that the force is slowly building up for the bicapped cube specimens, while the force of the bicapped square antiprisms quickly increases at the start of the test. This large difference could be explained by the number and length of the rigid rods of the different geometries. While the force is distributed over eight short rigid rods in the bicapped square antiprism specimens, the force is distributed over fewer and longer rods in the bicapped trigonal antiprism and bicapped cube specimens. The shorter rods in the bicapped square antiprism specimens are less susceptible to bending and buckling as compared to the longer rods present in the bicapped cube specimens. Similar results were found by El-Sayed et al. [38], who used SLM to manufacture diamond lattice structures with various strut thicknesses and lengths. The compressive strength was observed to increase with the strut thickness and to decrease with the strut length [38]. The different mechanical properties of our non-assembly mechanisms can be used to optimize the geometrical design of the implants to best suit the particular application at hand.

The mix of brittle and ductile fracture modes observed in the fractographs (Fig. 7) are typical for SLM parts in their as-built state [39,40]. This might be attributed to the high cooling [41] and solidification rates [40] and the small cross-sections of the parts perpendicular to the printing direction.

4.3. Future work

Although our non-assembly manufactured deployable implants show many advantages, some limitations should be addressed. SLM still has its limitations when it comes to the accuracy of printing. The smallest line thickness is dependent on the laser spot size and is found to be 200 μm with a laser beam size of 100 μm [42]. Since the revolute joints in our designs are used to enable the reconfiguration of the structures, it is challenging to reduce the size of the joint bearings significantly. These joint bearings are responsible for the circumdiameter of the retracted mechanisms, meaning that the diameter of the retracted mechanisms presented in this paper cannot be significantly reduced. We showed that different non-assembly deployable mechanisms can be made using single-step additive manufacturing. The designs and fabrication approaches presented in this study can be exploited to advance the applications of non-assembly mechanisms in other areas as well.

Although the fractographs show a combination of brittle and ductile surface fractures of our as-built structures, the brittle fracture mode was predominant. Many studies have been performed to improve the microstructure of as-built SLM specimens to make them more ductile [39,41,43]. It has been found that modifying the process parameters of the SLM process, post SLM heat treatments [39,41,43] and hot isostatic pressing (HIP) [39] can be used to relieve stresses and to reduce interior defects that are present in the SLM manufactured structures.

5. Conclusions

We designed and additively manufactured non-assembly deployable structures for application as orthopedic implants. SLM was used to manufacture these deployable structures from a medical grade titanium alloy that is widely used for the fabrication of orthopedic implants. SLM enables the integration of revolute joints, wavelike elements, rigid rods, and mechanical constraints. Additionally, this approach made the assembly of different components after manufacturing redundant and only the removal of the support structures and ultrasonic cleaning were required to make the deployable structures functional. Various geometries with different lengths for the rigid and wavelike rods were mechanically tested to determine the forces required to deploy the structures and to determine their failure loads. The porous structure of such implants is advantageous for bone ingrowth while their ability to reconfigure from an elongated to a load-bearing structure enables implantation using minimally invasive surgery. As compared to other implants that have been manufactured using SLM, the main advantage of these mechanisms is their ability to change their configuration. However, since the mechanisms reported here are the first SLM manufactured deployable non-assembly bone substitutes, future studies are required to further develop such mechanisms and to make them suitable as orthopedic implants.

CRedit authorship contribution statement

M.A. Leeflang: Conceptualization, Methodology, Writing – original draft, Writing – review & editing. **F.S.L. Bobbert:** Methodology, Data curation, Formal analysis, Validation, Visualization, Writing – original draft, Writing – review & editing. **A.A. Zadpoor:** Supervision, Writing – review & editing.

Declaration of Competing Interest

The authors declare that they have no known competing financial interests or personal relationships that could have appeared to influence the work reported in this paper.

Acknowledgments

The research leading to these results has received funding from the

European Research Council under the ERC grant agreement no. [677575].

References

- [1] M. Ansari, Bone tissue regeneration: biology, strategies and interface studies, *Prog. Biomater.* 8 (2019) 223–237.
- [2] J.J. Li, C.R. Dunstan, A. Entezari, Q. Li, R. Steck, S. Saifzadeh, A. Sadeghpour, J. R. Field, A. Akey, M. Vielreicher, A novel bone substitute with high bioactivity, strength, and porosity for repairing large and load-bearing bone defects, *Adv. Healthc. Mater.* 8 (8) (2019), 1801298.
- [3] C. Laurencin, Y. Khan, S.F. El-Amin, Bone graft substitutes, *Expert Rev. Med. Devices* 3 (1) (2006) 49–57.
- [4] Y. Yu, Y. Wang, W. Zhang, H. Wang, J. Li, L. Pan, F. Han, B. Li, Biomimetic periosteum-bone substitute composed of preosteoblast-derived matrix and hydrogel for large segmental bone defect repair, *Acta Biomater.* 113 (2020) 317–327.
- [5] C. Delloye, Tissue allografts and health risks, *Acta Orthop. Belg.* 60 (1994) 62–67.
- [6] S. Sahmani, A. Khandan, S. Esmaeili, S. Saber-Samandari, M.G. Nejad, M. Aghdam, Calcium phosphate-PLA scaffolds fabricated by fused deposition modeling technique for bone tissue applications: fabrication, characterization and simulation, *Ceram. Int.* 46 (2) (2020) 2447–2456.
- [7] Y. Lai, H. Cao, X. Wang, S. Chen, M. Zhang, N. Wang, Z. Yao, Y. Dai, X. Xie, P. Zhang, Porous composite scaffold incorporating osteogenic phytochemical icaritin for promoting skeletal regeneration in challenging osteonecrotic bone in rabbits, *Biomaterials* 153 (2018) 1–13.
- [8] S.K. Nandi, G. Fielding, D. Banerjee, A. Bandyopadhyay, S. Bose, 3D-printed β -TCP bone tissue engineering scaffolds: effects of chemistry on in vivo biological properties in a rabbit tibia model, *J. Mater. Res.* 33 (14) (2018) 1939–1947.
- [9] A. Atee, Y. Li, M. Brandt, C. Wen, Ultrahigh-strength titanium gyroid scaffolds manufactured by selective laser melting (SLM) for bone implant applications, *Acta Mater.* 158 (2018) 354–368.
- [10] Y. Li, Y. Ding, K. Munir, J. Lin, M. Brandt, A. Atrens, Y. Xiao, J.R. Kanwar, C. Wen, Novel β -Ti35Zr28Nb alloy scaffolds manufactured using selective laser melting for bone implant applications, *Acta Biomater.* 87 (2019) 273–284.
- [11] H. Kolkens, K. Lietaert, T. van der Sloten, B. Pouran, A. Meynen, G. Van Loock, H. Weinans, L. Scheys, A.A. Zadpoor, Mechanical performance of auxetic meta-biomaterials, *J. Mech. Behav. Biomed. Mater.* 104 (2020), 103658.
- [12] S. Wang, L. Liu, K. Li, L. Zhu, J. Chen, Y. Hao, Pore functionally graded Ti6Al4V scaffolds for bone tissue engineering application, *Mater. Des.* 168 (2019), 107643.
- [13] Y. Li, P. Pavanram, J. Zhou, K. Lietaert, P. Taheri, W. Li, H. San, M. Leeflang, J. Mol, H. Jahr, Additively manufactured biodegradable porous zinc, *Acta Biomater.* 101 (2020) 609–623.
- [14] C. Shuai, Y. Cheng, Y. Yang, S. Peng, W. Yang, F. Qi, Laser additive manufacturing of Zn-2Al part for bone repair: formability, microstructure and properties, *J. Alloy. Compd.* 798 (2019) 606–615.
- [15] P. Wen, L. Jauer, M. Voshage, Y. Chen, R. Poprawe, J.H. Schleifenbaum, Densification behavior of pure Zn metal parts produced by selective laser melting for manufacturing biodegradable implants, *J. Mater. Process. Technol.* 258 (2018) 128–137.
- [16] Y. Li, J. Zhou, P. Pavanram, M. Leeflang, L. Fockaert, B. Pouran, N. Tümer, K.-U. Schröder, J. Mol, H. Weinans, Additively manufactured biodegradable porous magnesium, *Acta Biomater.* 67 (2018) 378–392.
- [17] C. Gao, S. Li, L. Liu, S. Bin, Y. Yang, S. Peng, C. Shuai, Dual alloying improves the corrosion resistance of biodegradable Mg alloys prepared by selective laser melting, *J. Magnes. Alloy.* 9 (2021) 305–316.
- [18] F. Bär, L. Berger, L. Jauer, G. Kurtuldu, R. Schäublin, J.H. Schleifenbaum, J. F. Löffler, Laser additive manufacturing of biodegradable magnesium alloy WE43: a detailed microstructure analysis, *Acta Biomater.* 98 (2019) 36–49.
- [19] D. Carluccio, C. Xu, J. Venezuela, Y. Cao, D. Kent, M. Bermingham, A.G. Demir, B. Previtali, Q. Ye, M. Dargusch, Additively manufactured iron-manganese for biodegradable porous load-bearing bone scaffold applications, *Acta Biomater.* 103 (2020) 346–360.
- [20] Y. Li, H. Jahr, P. Pavanram, F. Bobbert, U. Puggi, X.-Y. Zhang, B. Pouran, M. Leeflang, H. Weinans, J. Zhou, Additively manufactured functionally graded biodegradable porous iron, *Acta Biomater.* 96 (2019) 646–661.
- [21] Y. Chen, J. Lu, Minimise joint clearance in rapid fabrication of non-assembly mechanisms, *Int. J. Comput. Integr. Manuf.* 24 (8) (2011) 726–734.
- [22] D. Bergqvist, G. Lowe, Venous thromboembolism in patients undergoing laparoscopic and arthroscopic surgery and in leg casts, *Arch. Intern. Med.* 162 (19) (2002) 2173–2176.
- [23] C.-H. Kuo, J.S. Dai, Robotics for Minimally Invasive Surgery: A Historical Review From the Perspective of Kinematics, *International Symposium on History of Machines and Mechanisms*, Springer, 2009, pp. 337–354.
- [24] V. Mais, S. Ajossa, S. Guerriero, M. Mascia, E. Solla, G.B. Melis, Laparoscopic versus abdominal myomectomy: a prospective, randomized trial to evaluate benefits in early outcome, *Am. J. Obstet. Gynecol.* 174 (2) (1996) 654–658.
- [25] S.S. Biere, M.L. van Berge Henegouwen, K.W. Maas, L. Bonavina, C. Rosman, J. R. Garcia, S.S. Gisbertz, J.H. Klinkenbijl, M.W. Hollmann, E.S. De Lange, Minimally invasive versus open oesophagectomy for patients with oesophageal cancer: a multicentre, open-label, randomised controlled trial, *Lancet* 379 (9829) (2012) 1887–1892.
- [26] R. Treuting, Minimally invasive orthopedic surgery: arthroscopy, *Ochsner J.* 2 (3) (2000) 158–163.

- [27] F. Bobbert, S. Janbaz, A. Zadpoor, Towards deployable meta-implants, *J. Mater. Chem. B* 6 (21) (2018) 3449–3455.
- [28] F. Bobbert, S. Janbaz, T. van Manen, Y. Li, A. Zadpoor, Russian doll deployable meta-implants: fusion of kirigami, origami, and multi-stability, *Mater. Des.* 191 (2020), 108624.
- [29] F. Calignano, Design optimization of supports for overhanging structures in aluminum and titanium alloys by selective laser melting, *Mater. Des.* 64 (2014) 203–213.
- [30] Y.-q Yang, X.-b Su, D. Wang, Y.-h Chen, Rapid fabrication of metallic mechanism joints by selective laser melting, *Proc. Inst. Mech. Eng. Part B J. Eng. Manuf.* 225 (12) (2011) 2249–2256.
- [31] A. Boschetto, L. Bottini, Manufacturability of non-assembly joints fabricated in AlSi10Mg by selective laser melting, *J. Manuf. Process.* 37 (2019) 425–437.
- [32] J.S. Cuellar, G. Smit, D. Plettenburg, A. Zadpoor, Additive manufacturing of non-assembly mechanisms, *Addit. Manuf.* 21 (2018) 150–158.
- [33] Y. Liu, J. Zhang, Y. Yang, J. Li, J. Chen, Study on the influence of process parameters on the clearance feature in non-assembly mechanism manufactured by selective laser melting, *J. Manuf. Process.* 27 (2017) 98–107.
- [34] A. Boschetto, L. Bottini, M. Eugeni, V. Cardini, G.G. Nisi, F. Veniali, P. Gaudenzi, Selective laser melting of a 1U cubesat structure, *Des. Addit. Manuf. Assem. Acta Astronaut.* 159 (2019) 377–384.
- [35] S. Leeftang, S. Janbaz, A.A. Zadpoor, Metallic clay, *Addit. Manuf.* 28 (2019) 528–534.
- [36] Y. Zhang, M. Tichem, F. van Keulen, Rotational snap-through behavior of multi-stable beam-type metastructures, *Int. J. Mech. Sci.* (2020), 106172.
- [37] M. Hajihosseinali, N. Arjmand, A. Shirazi-Adl, Effect of body weight on spinal loads in various activities: a personalized biomechanical modeling approach, *J. Biomech.* 48 (2) (2015) 276–282.
- [38] M.A. El-Sayed, K. Essa, M. Ghazy, H. Hassanin, Design optimization of additively manufactured titanium lattice structures for biomedical implants, *Int. J. Adv. Manuf. Technol.* 110 (9) (2020) 2257–2268.
- [39] X. Yan, S. Yin, C. Chen, C. Huang, R. Bolot, R. Lupoi, M. Kuang, W. Ma, C. Coddet, H. Liao, Effect of heat treatment on the phase transformation and mechanical properties of Ti6Al4V fabricated by selective laser melting, *J. Alloy. Compd.* 764 (2018) 1056–1071.
- [40] A. Moridi, A.G. Demir, L. Caprio, A.J. Hart, B. Previtali, B.M. Colosimo, Deformation and failure mechanisms of Ti-6Al-4V as built by selective laser melting, *Mater. Sci. Eng. A* 768 (2019), 138456.
- [41] C.-L. Li, J.-K. Hong, P. Narayana, S.-W. Choi, S.W. Lee, C.H. Park, J.-T. Yeom, Q. Mei, Realizing superior ductility of selective laser melted Ti-6Al-4V through a multi-step heat treatment, *Mater. Sci. Eng. A* 799 (2021), 140367.
- [42] F. Calignano, M. Lorusso, J. Pakkanen, F. Trevisan, E. Ambrosio, D. Manfredi, P. Fino, Investigation of accuracy and dimensional limits of part produced in aluminum alloy by selective laser melting, *Int. J. Adv. Manuf. Technol.* 88 (1–4) (2017) 451–458.
- [43] A. Popovich, V. Sufiiarov, E. Borisov, I.A. Polozov, Microstructure and Mechanical Properties of Ti-6Al-4V Manufactured by SLM, *Key Engineering Materials, Trans Tech Publ.*, 2015, pp. 677–682.